ADVANCED FUNCTIONAL MATERIALS
www.afm-journal.de

Dendri-LEC Family: Establishing the Bright Future for Dendrimer Emitters in Traditional and Graphene-Based Light-Emitting Electrochemical Cells

Luca M. Cavinato, Keiko Yamaoka, Sophia Lipinski, Vladimir Calvi, Dominique Wehenkel, Richard van Rijn, Ken Albrecht, and Rubén D. Costa**

A rational implementation and optimization of thermally activated delayed fluorescent (TADF) dendrimer emitters in light-emitting electrochemical cells (LECs) sets in the Dendri-LEC family. They feature outstanding stabilities (90/1050 h for green/yellow devices) that are comparable to the best green/yellow Ir(III)-complexes (450/500 h) and conjugated polymers (33/5500 h), while offering benefits of low-cost synthesis and easy upscaling. In particular, a fundamental molecular design that capitalizes on exchanging peripheral substituents (*tert*-butyl vs methoxy) to tune photophysical, electrochemical, morphological, and ion conductivity features in thin films is rationalized by temperature-dependent steady-state and time-resolved emission spectroscopy, cyclic voltammetry, atomic force microscopy, and electrochemical impedance spectroscopy techniques. Herein, a TADF mechanism associated to a reduced photoluminescence quantum yield, but an enhanced electrochemical stability and ion conductivity enables to clarify the reduced device efficiency and brightness (4.0 lm W^{-1}@110 cd m^{-2} vs 3.2 lm W^{-1}@55 cd m^{-2}) and increased stability (90 vs 1050 h) upon using methoxy groups. What is more, this substitution enables an excellent compatibility with biogenic electrolytes keeping device performances (1.9 lm W^{-1}@35 cd m^{-2} and 1300 h), while graphene-devices achieve on par figures to traditional indium–tin oxide-devices. Overall, this work establishes the bright future of dendrimer emitters toward highly stable and truly sustainable lighting sources.

1. Introduction

Dendrimers have attracted wide interest in both academia and industrial communities in the last decades.[1,2] They are described as branched polymers displaying an exact and controllable molecular weight and high solubility, which are common features of small molecules. Therefore, they are placed in the midway between the two worlds. Due to their high solubility, they are appealing for all the technologies that rely on wet fabrication techniques. Indeed, a proper molecular design has led to significant breakthroughs in solution processed organic light-emitting diodes (OLEDs), since their unique polarized electronic structure enables the design of thermally activated delayed fluorescent (TADF) materials.[3–7] Here, all the generated excitons in thin-film lighting are fully used by converting triplet excitons into singlet ones via an efficient reverse intersystem crossing (rISC) promoted by the small energy splitting of excited singlet and triplet states (ΔE_{ST}).[8] Indeed, dendrimers-based OLEDs have recently achieved external quantum efficiency (EQE) values near to 30%.[9,10]

L. M. Cavinato, S. Lipinski, R. D. Costa
Chair of Biogenic Functional Materials
Technical University of Munich
Schulgasse 22, 94315 Straubing, Germany
E-mail: ruben.costa@tum.de

K. Yamaoka, K. Albrecht
Institute for Materials Chemistry and Engineering
Kyushu University
6-1 Kasuga-Koen Kasuga-shi, Fukuoka 816-8580, Japan
E-mail: albrecht@cm.kyushu-u.ac.jp

V. Calvi, D. Wehenkel, R. van Rijn
Applied Nanolayers B.V.
Feldmannweg 17, 2628 CD Delft, The Netherlands

The ORCID identification number(s) for the author(s) of this article can be found under https://doi.org/10.1002/adfm.202302483

DOI: 10.1002/adfm.202302483

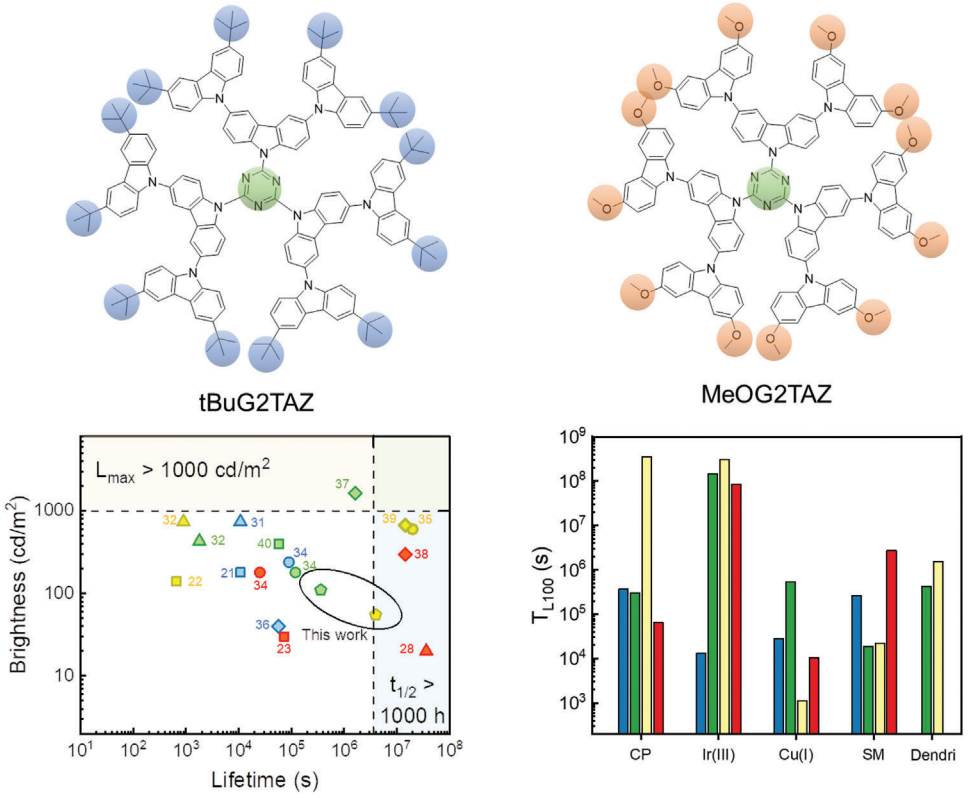

Figure 1. Top: chemical structures of the dendrimer-emitters (see names). Bottom-left: brightness (cd m^{-2}) and experimental device lifetime (s) of the state-of-art emitters LECs (circles: CPs,[34,35] diamonds: Ir(III)-iTMCs,[36–39] squares: Cu(I)-iTMCs,[21–23,40] triangles: small molecules[28,31,32]) in different regions of the visible spectrum highlighted by the color of the symbol. Dendrimer-based LECs presented in this work are highlighted with colorful pentagons. Bottom-right: comparison of extrapolated lifetime at 100 cd m^{-2} (s) (T_{L100})[41] of different type of emitters divided by device chromaticity highlighted by the color of the bars.

In this context, it is surprising that a rationalization toward optimizing dendrimers-based light-emitting electrochemical cells (LECs) has not been reported yet.[11] LECs are the simplest thin-film lighting device featuring a single and ion-based active layer prepared via low-cost solution-based technologies using air-stable electrodes.[12,13] Upon biasing, LECs exhibit efficient ion-assisted charge injection by forming electric double layers (EDLs) at the electrode interfaces and ion-controlled growing of the p-/n-doped fronts, while the electron–hole recombination occurs at the intrinsic neutral zone (*i*) of a dynamically formed p–*i*–n junction.[14] Therefore, LECs show a high thickness tolerance, allowing fabrication of flexible substrates and/or with complex 3D shapes.[15] In addition, their simple architecture facilitates the fabrication of disposable or reusable devices.[16,17] All-in-all, LECs are shining for smart lighting applications and sustainability aspects.[18] Concerning the latter, the best performing devices with average lifetimes of hundreds of hours at >500 cd m^{-2} with luminous power efficiencies of >10 lm W^{-1} are, however, based on either rare-earth emitters like ionic Iridium(III) complexes or expensive conjugated polymers (CPs)—**Figure 1**; and Table S1 (Supporting Information).[19,20] In the last decades, alternative emitters have been investigated. On one hand, many efforts have been realized developing LECs based on Cu(I) complexes. Today, the best performing blue,[21] yellow,[22] and red[23] Cu(I) based LECs feature brightness of 180/140/30 cd m^{-2} associated with lifetime of 25/0.2/20 h, respectively. While they are not competitive for the mid-/low-energy visible region, they have recently outperformed the Ir(III) based counterpart in the blue region.[24] On the other hand, organic small molecules have been proposed spanning a wide palette of families, namely: benzothiadizole,[25] perylene,[26] nanographene,[27,28] pentacene,[29] phorphyrin,[30] and carbazole-based TADF molecule,[31,32] among others. In the blue and yellow region good brightness (>500 cd m^{-2}) with modest lifetime (<5 h)[31,32] have been achieved, while in the red one high stability (<10^4 h) have been achieved with poor brightness level (<30 cd m^{-2}).[28] Hence, an ideal family of sustainable and low-cost emitter has not been established.

Herein, we rationalize the implementation and optimization of carbazole-dendrimer TADF emitters as a new family of LEC emitters, i.e., Dendri-LECs, emphasizing their most significant achievements and limitations in ionic-based lighting devices. In detail, the archetypal dendrimer **tBuG2TAZ** has been chosen as reference,[33] while the novel dendrimer **MeOG2TAZ** has been synthesized and characterized to demonstrate the easy tunability of the device chromaticity and outstanding enhancement in device stability. While the **tBuG2TAZ** show a TADF mechanism associated to photoluminescence quantum yield (PLQY) in thin films of ≈60% and a bright green electroluminescence in traditional LECs, i.e., 4.0 lm W^{-1}@110 cd m^{-2}, the device stability is moderate compared to the prior-art LEC-emitters due to

Table 1. Electrochemical properties of dendrimers in DMF solution. Oxidation and reduction potentials are referenced to $Cp_2Fc^{+/0}$.

	Oxidation			Reduction					
Dendrimer	$E_{1/2}$ [V]	i_{pa}/i_{pc}	ΔE_p [mV]	$E_{1/2}$ [V]	i_{pa}/i_{pc}	ΔE_p [mV]	E_{HOMO} [a)] [eV]	E_{LUMO} [a)] [eV]	$\Delta E_{HOMO\text{-}LUMO}$ [eV nm^{-1}]
tBuG2TAZ	0.69	2.79	75.7	−1.84	1.00	95.5	−5.45	−2.99	2.46/504
MeOG2TAZ	0.37	1.71	79.1	−1.89	0.78	70.4	−5.15	−2.96	2.19/566

[a)] Calculated from oxidation/reduction potential of cyclic voltammetry as reported in ref. [43].

the electrochemical degradation in operando, i.e., ≈90 h or 103 h@100 cd m^{-2} (T_{L100}) as shown in Figure 1. In stark contrast, the **MeOG2TAZ**-based LECs achieved moderate yellow emission (3.2 lm W^{-1}@55 cd m^{-2}) due to a lower PLQY in thin film (≈30%), while the device stability is however outstanding reaching over 1050 h (>1.5 months) or T_{L100} of almost 450 h that is among the best reported yellow emitters to date—Figure 1. Finally, this performance hold in indium–tin oxide (ITO)-free LECs with graphene-based electrodes and novel biogenic cellulose-based electrolytes,[13] highlighting their potential to realize truly sustainable and highly performing lighting devices in the near future.

2. Result and Discussion

2.1. Synthesis and Characterization

tBuG2TAZ was prepared following our reported protocol,[33] while the synthesis of **MeOG2TAZ** was adapted from the procedure reported elsewhere for standard N-arylation reaction.[33,42] The targeted compound was isolated as yellow solids in good yields (66%)—see the Experimental Section for details; and **Figures** S1–S3 (Supporting Information).

In dry toluene solution, both compounds show a similar absorption spectrum shape with three bands centered at the high-energy region of ≈300 and 350 nm, which are related to the π–π transitions of each moiety, and above 400 nm that is attributed to the intramolecular charge-transfer transition from carbazole to triazine core—**Figure** S4 (Supporting Information). In line with the electron donating groups attached to the **MeOG2TAZ**, the whole absorption spectrum is red-shifted. This is also reflected in the photoluminescence (PL) features with a structureless emission band centered at ≈490 and 515 nm for **tBuG2TAZ** and **MeOG2TAZ**, respectively, **Figure** S4 (Supporting Information). This is typically ascribed to the donor effect of the peripheral methoxy substituents that destabilizes the highest occupied molecular orbital (HOMO) level, reducing the optical bandgap—**Table 1**. What is more, the presence of a smaller terminal donor groups on the peripheral carbazole moieties induces a reduction of the PLQY from 80% (**tBuG2TAZ**) to 52% (**MeOG2TAZ**), in solution. In line with the energy gap law, the reduction of the PLQY might be related to the enhanced nonradiative rate pathways related to structural changes (i.e., steric hindrance, intermolecular weak interactions, vibrational modes, etc.) as well as electronic changes (i.e., Franck-Condon overlapping, vibrational coupling, etc.). This trend is also noted in thin-films, in which a more thoughtful spectroscopic study is presented, vide infra.

Finally, the electrochemical features in solution were investigated via cyclic voltammetry, see the Experimental Section; and **Figures** S5 and S6 (Supporting Information); and Table 1. In short, **tBuG2TAZ** showed a quasi-reversible oxidation wave at 0.69 V and a reversible reduction wave at −1.84 V, while **MeOG2TAZ** showed quasi#x02010;reversible oxidation and reduction waves at 0.37 and −1.89 V, confirming the above spectroscopic features. More importantly, the **MeOG2TAZ** shows an enhanced electrochemical stability upon repetitive cycles than the **tBuG2TAZ**, highlighting their potential use for LECs.

2.2. Photophysical Properties in Thin Films

Concerning film-forming behavior, both tested dendrimers show high solubility in organic solvents, vide supra, leading to homogenous thin films upon spin coating. The morphology of the films was monitored via atomic force microscopy (AFM) in a 100 μm^2 area. The root mean square (RMS) roughness of pristine thin films ranges from 410 to 259 pm for **tBuG2TAZ** and **MeOG2TAZ**, respectively, **Figure** S7 (Supporting Information).

In good agreement with the literature and the PL in solution,[33] **tBuG2TAZ**-/**MeOG2TAZ**-based films showed broad emission band centered at 510/565 nm associated to average excited state lifetimes (<τ>)/PLQY values of 121 ns/63% and 112 ns/26%, respectively—**Figure 2** and **Table 2**. In both cases, the transient PL decay curve points to the presence of both short and long lifetime components attributable to a TADF process.[33] In detail, Figure 2d,e shows streak images of both films at 300 K, providing visual confirmation of the time-dependent intensities of the prompt (t ≈ 0 ns) and delayed fluorescence (t >40 ns) components. The delayed components can be assigned to the fluorescence via rISC. While the two components are isoenergetic in **MeOG2TAZ**-film, a slight red-shift was observed for **tBuG2TAZ**-films. This phenomenon has been already reported in several studies,[44–47] and it is commonly attributed to a fast fluorescence process that occur immediately after the rISC. Here, the nuclear configuration of the singlet excited state formed through the rISC is affected by that of the triplet excited state. As a result, the Franck–Condon factor of the delayed component would be different to that of the prompt component. The high radiative constant rate (k^S_r) exhibited by **tBuG2TAZ**-films further supports this finding, i.e., 21.8×10^6 s^{-1}.

The temperature-dependent PL behavior, i.e., changes in emission band shape and <τ> upon increasing the temperature from 77 to 300 K—of the **MeOG2TAZ**-film was further investigated—**Figure 3**. The temperature increase from 77 to 300 K leads to a hypsochromic shift of the E_{0-0} band—≈12 nm or 0.045 eV,

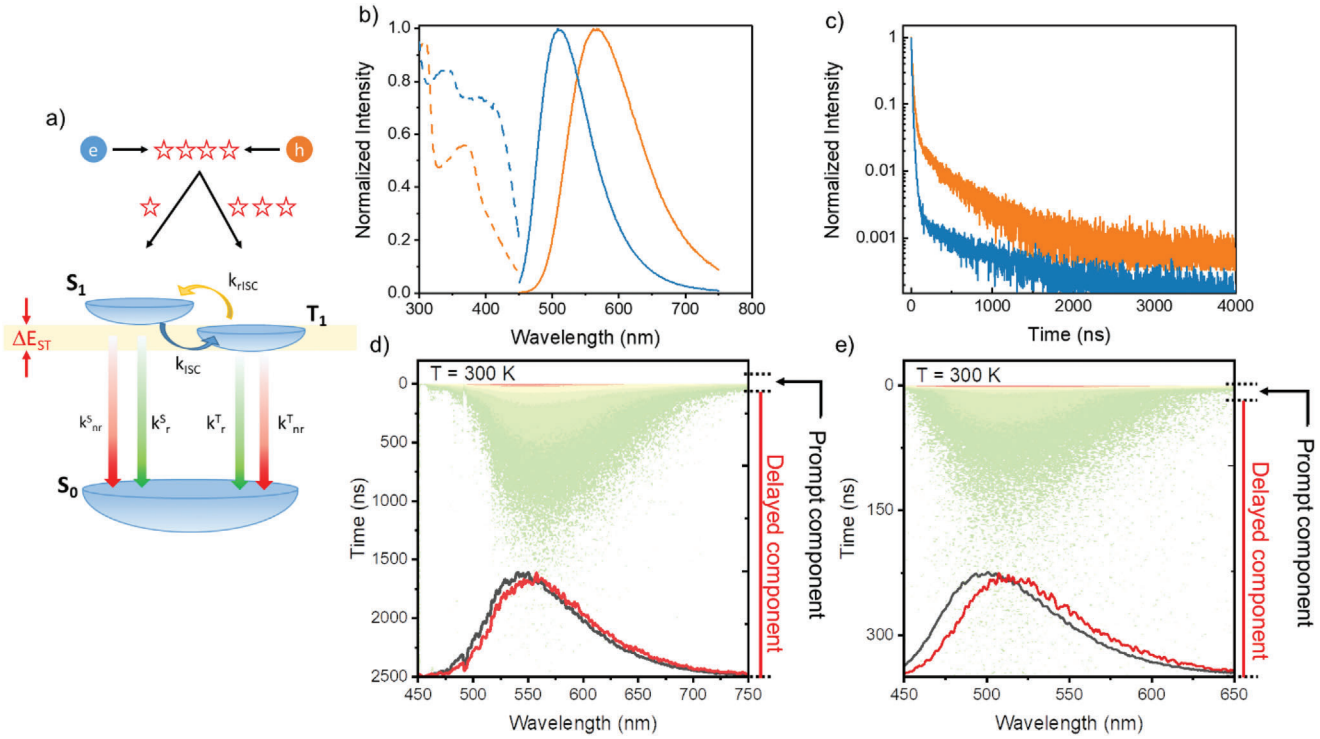

Figure 2. a) Simplified Jablonski diagram describing the possible pathways after electron–hole recombination. k^S_{nr}, k^S_r, k^T_{nr}, and k^T_r are the nonradiative and radiative constants of the singlet and triplet state, respectively. k_{ISC} and k_{rISC} are the ISC and rISC rate constants between the singlet and the triplet state. ΔE_{ST} is the difference of energy between the aforementioned states. b) Excitation (dashed line) and emission (solid line) of **MeOG2TAZ**- (orange) and **tBuG2TAZ**- (blue) films. c) Corresponding excited state decay profiles measured with a picosecond laser (λ_{exc} = 372 nm) at 300 K. d,e) Streak image and PL spectra of **MeOG2TAZ**- d) and **tBuG2TAZ**- e) films at 300 K. The PL spectra are resolved into prompt ($t \approx 0$ ns) and delayed components (>40 ns).

Table 2. Photophysical properties of dendrimer-based thin films. Constant rates extrapolated according to model reported in ref. [54].

Dendrimer	Additives	λ_{em} [nm]	ϕ[a)] [%]	τ_F/ϕ_F [ns/%]	τ_{DF}/ϕ_{DF} [ns/%]	k^S_r ($\times 10^6$) s^{-1}	k_{ISC} ($\times 10^6$) s^{-1}	k_{rISC} ($\times 10^6$) s^{-1}	ΔE_{ST} [eV]
tBuG2TAZ	—	510	63	19.2/41	536/22	21.8	11.3	3.1	0.05
	PS-THA	515	77	12.9/42	344/35	31.7	27.8	3.0	0.04
MeOG2TAZ	—	565	26	22.6/14	322/12	6.6	5.1	3.7	0.05
	CA-THA	556	22	22.7/13	299/9	5.7	3.7	4.4	0.06
	PS-THA	556	24	22.4/14	330/10	6.3	4.5	3.8	0.05

[a)] Measured in inert atmosphere at 300 K.

implying that the emission may arise from two emissive excited states in thermal equilibrium. Importantly, $<\tau>$ values drastically changes spanning from 0.16 ms at 77 K to 112 ns at room temperature, and its temperature dependence follows a Boltzmann-type equation[48,49] — see the Supporting Information for further details. A good fit ($R^2 > 0.99$) in the 77–300 K temperature range was obtained. The extrapolated values are $<\tau>_S$ = 100 ns, $<\tau>_T$ = 234 µs, and ΔE_{ST} = 0.049 eV. Commonly,[44,50,51] when modeling the photophysical parameters of organic TADF emitters, k^S_r, k^S_{nr}, and k_{ISC} are assumed much greater than k^T_{nr} and k_{rISC}, while k^T_r is neglected. Within this boundary conditions, the methods proposed by Adachi's group[44,52] and Monkman's group[53–55] to estimate k_{rISC} and ΔE_{ST} can be applied—see the Supporting Information for both derivations and the results. In detail, **MeOG2TAZ**-films feature k^S_r, k_{ISC}, k_{rISC}, and ΔE_{ST} extrapolated values from time-resolved spectroscopic data of 6.6 × 10^6 s^{-1}, 5.1 × 10^6 s^{-1}, 3.7 × 10^6 s^{-1}, and 0.05 eV, respectively, while **tBuG2TAZ**-films exhibited k^S_r, k_{ISC}, k_{rISC}, and ΔE_{ST} of 21.8 × 10^6 s^{-1}, 11.3 × 10^6 s^{-1}, 3.1 × 10^6 s^{-1}, and 0.05 eV, respectively. What is more, the estimated activation energy of rISC process is in good agreement with the one expected using the Boltzmann's model and between the different methods applied, validating the applied analytical derivation—Table 2; and **Table** S2 (Supporting Information). At this point, it is important to point out that when k^S_{nr} is considered, thek $>_{ISC}$ of **MeOG2TAZ**-films is one-order of magnitude lower than the commonly reported values, i.e., ≈20 × 10^6 s^{-1},[6,33,42] which are, however, ascribed to TADF materials that

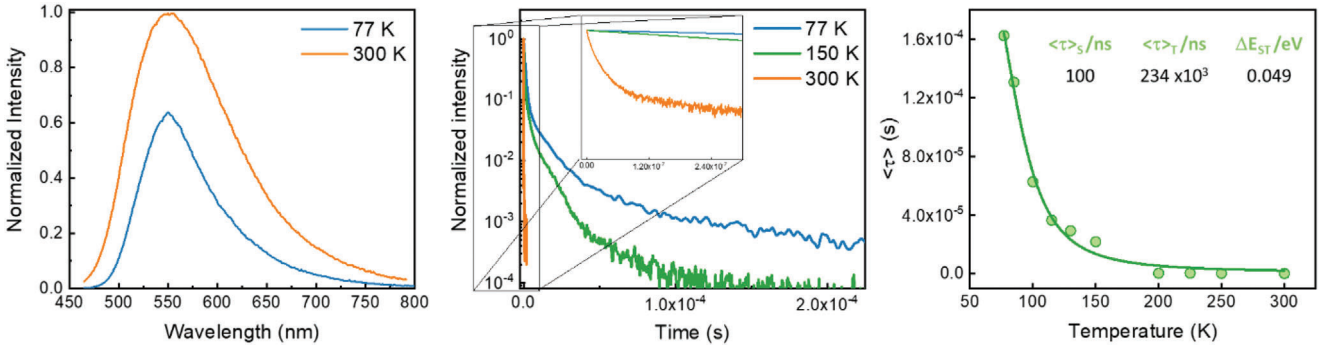

Figure 3. Emission spectra (left) and excited-state decay profiles (middle) of **MeOG2TAZ**-films recorded at different temperatures. Right: average τ values of **MeOG2TAZ**-films versus temperature. The solid lines represent the fit curves according to Boltzmann's equation, while the extrapolated parameters are provided as inset.

exhibit a PLQY of nearly 100%. Therefore, quenching at room temperature is negligible. By contrast, **MeOG2TAZ**-based thin films show a PLQY< 30% and the nonradiative pathways are not negligible, i.e., k^{S}_{nr} 32.4 × 10^6 s^{-1}, causing a shortening of the delayed lifetime at 300 K.

Finally, in donor–acceptor TADF emitters, the constant rates of the photophysical processes depend on the dihedral angle between donor and acceptor moieties. These angles exist as distribution in thin films, resulting in a wide distribution in the constant rates that are difficult to quantify.[56] Here, we report the average values of those distributions.

After confirming a TADF emission mechanism, we turned our attention on the influence of ionic additives employed in the active layer of the final device, vide infra , as it has been demonstrated that the presence of ionic additives can alter similarly the spin-vibronic coupling.[21,31,57] Thus, morphology and photophysical response of films embedding dendrimers and ion polyelectrolyte was also studied. Since the appropriate selection of the electrolyte is crucial to meet high performing LECs, we explored a wide variety of traditional ion-based electrolytes in LECs, namely PEO-based electrolytes, ionic liquids, inorganic salts, etc. Among them, we selected the combinations leading to thin films with RMS roughness <1 nm, **Figure** S7 (Supporting Information). In detail, for **tBuG2TAZ** and **MeOG2TAZ** blended with polystyrene (PS):tetrahexylammonium tetrafluoroborate (THA) in mass ratio 1:2 (PS-THA) was optimal, allowing a direct device performance comparison, while **MeOG2TAZ** was also compatible with cellulose acetate (CA):THA in mass ratio 1:1 (CA-THA), enabling further optimization toward sustainable LECs, vide infra.

PS-THA films featured the same structureless emission centered at 515 and 556 nm for **tBuG2TAZ**- and **MeOG2TAZ**-films, respectively. Noteworthy, while no change in the emission maximum has been recorded for the former, the latter shows a slight blueshift (≈10 nm) that can be attributed to a change of the polar environment surrounding the emitter. The good matching between the excitation spectra infers that the same excited state is involved in the emission process, independent of the type of electrolyte, **Figure** S8 (Supporting Information). What is more, the time-resolved spectroscopic data show the presence of both short and long components in all the cases, **Figures** S9 and S10 (Supporting Information). Thus, regardless of the electrolyte, the TADF expression is retained and k_{rISC} is slightly enhanced, Table 2; and Table S2 (Supporting Information). In particular, for **MeOG2TAZ**-films the constant rates k^{S}_{r}, k_{rISC}, and k_{ISC} are in the same order of magnitude. This could be attributed to the importance of k^{S}_{nr} in such systems that act as leveling agent toward the small differences induced by the electrolyte on the spin-vibronic coupling of the dendrimers. In contrast, the presence of PS-THA in **tBuG2TAZ**-films enhances both k^{S}_{r} and k_{ISC} and, consequently, more efficient devices are expected upon using the ion electrolyte.

2.3. Electroluminescent Properties on LECs with Traditional Glass/ITO Substrates

Next, LECs were fabricated with a double-layered architecture ITO/PEDOT:PSS (50 nm)/active layer (70–90 nm)/Al (90 nm) and analyzed by monitoring the luminance, color, and electrical behavior over time. At first, the devices were driven under pulsed current density of 10 mA cm^{-2}, 1 kHz block wave, 50% duty cycle. In line with the PL features in thin films and the electroluminescence (EL) in OLEDs,[33] **tBuG2TAZ:PS-THA** devices showed a green electroluminescence response consisting of a broad and structureless band centered at 525 nm, which is associated to x/y CIE color coordinates of 0.27/0.50 and a color purity of 0.5. Noteworthy, no color corruption was noted over the entire measurement timespan—**Figure 4**a,d, indicating the lack of i) quenchers and/or carrier traps, ii) strong polarization under electric field, and/or *iii)* microcavity and scattering effects.[27,58,59] In addition, the devices showed the typical LEC behavior: an initial voltage (4.9 V) that exponentially reduces to a plateau around 3.5 V, while the luminance rises from an initial value of 44 cd m^{-2} to a maximum of 110 cd m^{-2} along with a maximum luminous power efficiency value of 4.0 lm W^{-1}—**Table 3**. The quick (<20 min) decrease of the average voltage is related to the electrochemical doping promoted by the formation of EDLs at the electrode interfaces, while the lack of a stable voltage plateau indicates a slow electrochemical degradation, i.e., over oxidation/reduction processes as highlighted by the electrochemical assays, vide supra.[30] After 50 h, a drop in the luminance level was recorded, while the average voltage continuously raised, ending up in a $t_{1/2}$ (time to reach half of the maximum luminance) of ≈90 h. In stark contrast,

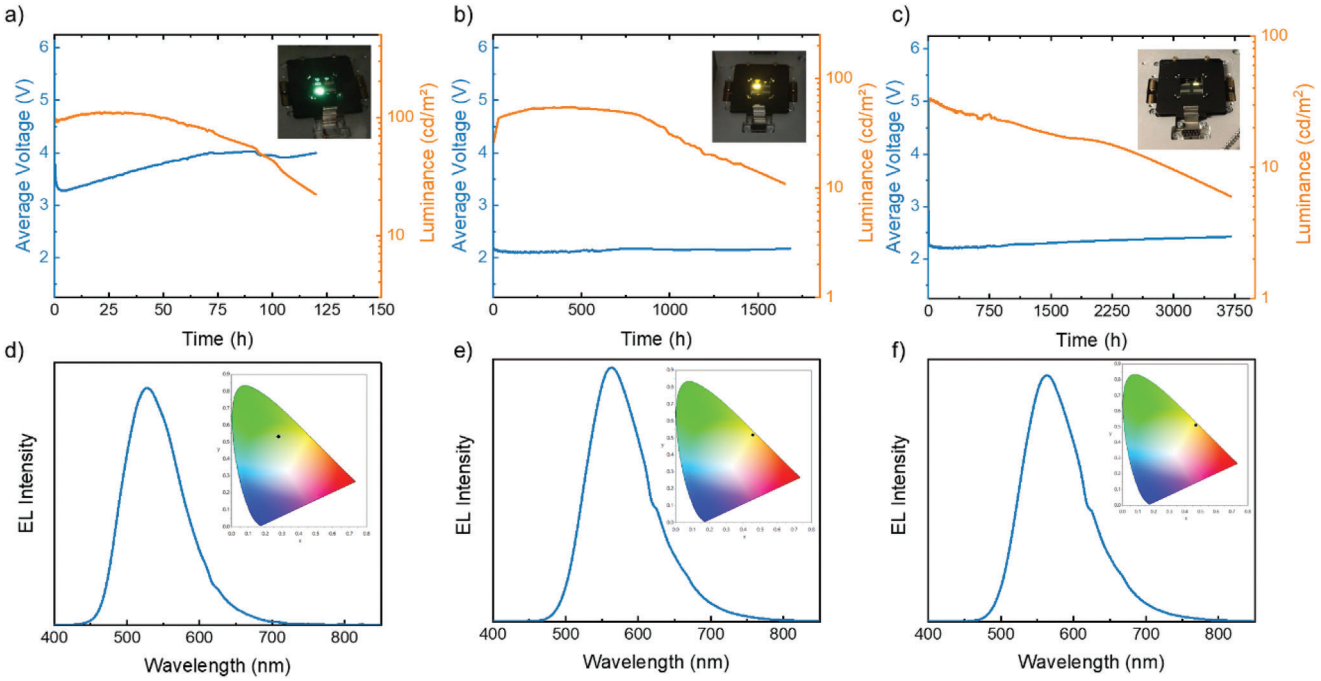

Figure 4. Top: luminance (orange) and average voltage (blue) for **tBuG2TAZ:PS-THA**- a), **MeOG2TAZ:PS-THA**- b), and **MeOG2TAZ:CA-THA**- c) devices measured using a pulsed current density of 10 mA cm^{-2}. Bottom: d-f) corresponding electroluminescence spectra of the above-mentioned devices. The insets show the associated *x*/*y* CIE color coordinates.

Table 3. Figures-of-merit of traditional LECs at pulsed current driving.

Dendrimer	Additive	Initial Voltage [V]	L_{max} [cd m^{-2}]	Efficacy [cd A^{-1}]	Power Efficiency [lm W^{-1}]	$t_{1/2}$ [h]	E_{tot} [J]	T_{L100} [h]	ϵ_r	σ [nS m^{-1}]
tBuG2TAZ	PS-THA	4.9	110	2.2	4.0	90	5.71	103	7.4	160
MeOG2TAZ	PS-THA	3.1	55	1.1	3.2	1050	98.3	428	6.8	548
	CA-THA	3.7	35	0.7	1.9	1300	88.2	270	10.3	392

MeOG2TAZ-LECs showed a yellow electroluminescence response consisting of a structureless band centered at 565 nm associated with x/y CIE color coordinates of 0.47/0.51 and color purity of 0.95, regardless the nature of the employed ion electrolyte, Figure 4b,c,e,f. Likewise **tBuG2TAZ** devices, no color corruption was noted in operando and the E_{0-0} band of PL/EL spectra holds constant—≈2.5 eV—inferring that the same excited state is involved. While the voltage profile is similar for both electrolytes, reaching a plateau around 2.1–2.3 V in a similar time range (<20 min), **MeOG2TAZ:PS-THA** and **MeOG2TAZ:CA-THA** devices showed a maximum luminance of 55 and 35 cd m^{-2}, a maximum luminous power efficiency of 3.2 and 1.9 lm W^{-1}, and $t_{1/2}$ of 1050 and 1300 h, respectively—Table 3. Noteworthy, with both electrolytes, the achieved $t_{1/2}$ is in the same order of magnitude of the best performing yellow LEC-emitters to date—4000 and 5500 h for Ir(III) complexes and CPs, respectively; Figure 1; and Table S1 (Supporting Information).

With this data at hand, we can rationalize the difference between **MeOG2TAZ** versus **tBuG2TAZ** devices in terms of i) a reduced luminance that is in line with the lower PLQYs exhibited in thin films, i.e., ≈30% versus 77%, Table 2, and *ii)* enhanced device stabilities as the electrochemical stress is alleviated, vide supra. However, the direct comparison between device stabilities at different luminance levels is not fair. The common parameters that have been introduced for this purpose are the total emitted energy (E_{tot}; the integral of the radiant flux vs time from t = 0 to >t = 1/5 of the maximum irradiance)[60] and the stability extrapolated at 100 cd m^{-2} (T_{L100}).[41] While **tBuG2TAZ**-LECs exhibited E_{tot} of 5.71 J and T_{L100} of 103 h, **MeOG2TAZ**-LECs showed values as high as 98.3/88.2 J and 428/270 h for PS-THA-/CA-THA-based electrolytes, respectively. Hence, the device stability of **MeOG2TAZ** is almost 20-fold higher in term of E_{tot} than **tBuG2TAZ** devices, Table 3.

As a final note, we turned our attention on the differences in the brightness temporal evolution, in which PS-THA devices shown a plateau brightness and CA-THA devices exhibited a continuous very slow decay, Figure 4. If degradation phenomena are excluded, the position of the emissive intrinsic (i) neutral region is related to a good balance of p-/n-type doping derived from: i) balanced electron/hole injection ($\Delta E_e \approx \Delta E_h$), ii) similar

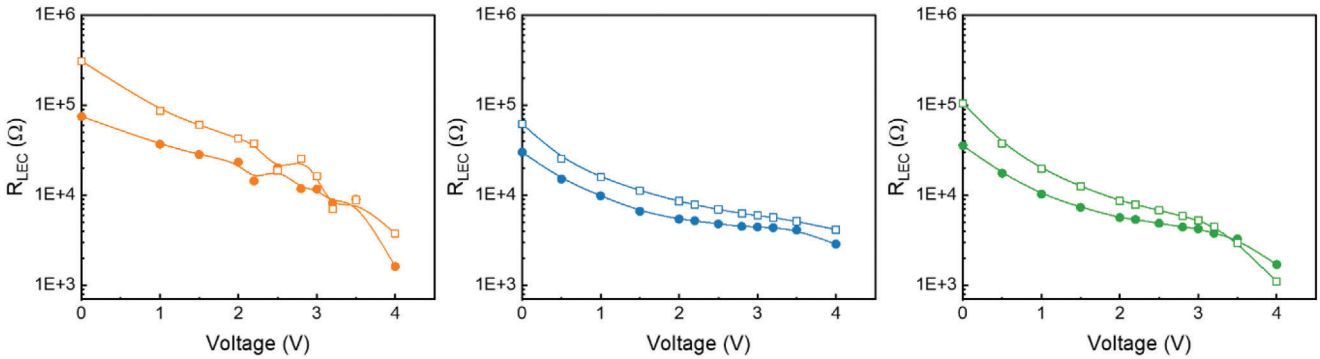

Figure 5. Changes in R_{LEC} parameter of **tBuG2TAZ:PS-THA**-(left), **MeOG2TAZ:PS-THA**-(middle), and **MeOG2TAZ:CA-THA**-(right) based LECs. The full circles and the empty circles refer to fresh and used devices, respectively.

electron/hole mobilities ($\mu_e \approx \mu_h$), and/or iii) analogous ionic mobilities ($\mu_c \approx \mu_a$), while a brightness decrease is associated with a slow movement of the emissive zone and/or narrowing of the intrinsic (i) neutral region.[14,61] In devices with PS-THA-based electrolytes, the difference in the initial applied voltage—Table 3—might be related to different hole injection barriers between **tBuG2TAZ** and **MeOG2TAZ** that are reduced compared to those for electron injection, vide supra, suggesting that both devices will show an unbalanced electron–hole behavior. Here, electrochemical impedance spectroscopy (EIS) aids us to monitor the kinetics of EDLs formation and to calculate the overall ionic conductivity (σ) and dielectric constant (ϵ_r) of the active layers, see the Experimental Section for further details; Table 3. Both devices showed ϵ_r values of ≈7, that is, a similar tendency of forming EDLs is expected, while σ is almost 4-times enhanced in **MeOG2TAZ** devices, i.e., 548 versus 160 nS m^{-1}, facilitating the formation and growing of stable p-/n-doped regions that prevent electrochemical degradation as well as reduction of *i* zone. This is confirmed by static EIS assays at bias voltages ranging from 0 to 4 V with a frequencies scan of 10^0–10^6 Hz.[41] In general, all the devices show similar Nyquist plots consisting of a single semicircle that was fitted with the equivalent electric circuit depicted in Figure S11 (Supporting Information). The changes in the slope of the R_{LEC} versus voltage profile are shown in **Figure 5**. At the low voltage regime, the decrease in R_{LEC} is attributed to the dynamics of EDLs formation that is more favorable for **MeOG2TAZ:PS-THA** devices than those with **tBuG2TAZ:PS-THA**, i.e., lower R_{LEC} values and higher decay slope. Upon changing the electrolyte to CA-THA, a similar static EIS behavior is noted; though σ is slightly reduced and ϵ_r is increased, Table 3, indicating that EDLs formation should be similar. At the high voltage regime, ohmnic contacts are established and the reduction and/or shifting of the intrinsic region are the dominant processes due to uneven growing of the doped regions. Here, **tBuG2TAZ** devices featured a dramatic reduction of R_{LEC}, while this is very small for both **MeOG2TAZ** devices. This explains that the luminance plateau is much shorter for **tBuG2TAZ:PS-THA** in the studied series, Table 3, while the impact of the electrolytes in **MeOG2TAZ** devices requires a deeper study about the ion and electronic mobility balance as pointed out by the recent works of Edman's and Hany's groups.[14,61] Finally, the EIS static analysis of all used devices showed a higher resistance profile with respect of fresh ones, Figure 5, pointing out that electrochemical degradation is responsible of the final device stability.[48]

2.4. Electroluminescent Properties of LECs with Glass/Graphene Substrates

Considering the excellent stability of **MeOG2TAZ**-based LECs using biogenic electrolytes, i.e., CA-THA,[13] we decided to prepare ITO-free LECs to demonstrate the potential of this family toward truly sustainable LECs. Here, wafer-scale chemically vapor deposited single-layered graphene (SLG) was synthesized and transferred on optical glass substrates, see the Experimental Section for further details. Although superior in terms of quality and uniformity, SLG has a low intrinsic charge concentration compared to multilayered graphene (MLG), resulting in high sheet resistance.[62] Thus, we formed a MLG anode via repetitive (three times) transfer of SLG on cleaned glass substrates. The successful transfer was confirmed via Raman Spectroscopy, Figure S12 (Supporting Information), and AFM topography analysis before and after active layer deposition, Figure S13 (Supporting Information). In detail, upon transfer of 3 SLG the ratio between I_{2D}/I_G peaks decrease from 1.27 (SLG) to 0.54 (MLG) indicating that subsequent transfers does not damage the basal plane of graphene. AFM mapping reveals that RMS increase from 438 pm (SLG) to 1752 pm (MLG) inferring that transferring several layers of graphene leads to trapping of undesirable material in between the layers, which causes increase of roughness.[62] However, they are fine for graphene-LEC fabrication. As described in the Experimental Section, the final device architecture consists of a PEDOT:PSS (150 nm), an active layer (70–90 nm) with an homogenous morphology with a total RMS 428 pm, and a final layer of Al (90 nm) as cathode. Both ITO/PEDOT:PSS/**MeOG2TAZ:CA-THA**/Al and graphene/PEDOT:PSS/**MeOG2TAZ:CA-THA**/Al were driven at pulsed 100 mA cm^{-2} (1 kHz, block-wave), **Figure 6**, since the MLG graphene conductivity and the graphene PEDOT:PSS interface is not optimized to allow operation at lower applied current compliances; this is currently on going in our laboratories. Both devices showed the same instantaneous yellow emission and a similar electronic behavior that leads to comparable luminance and power efficiency profiles. Indeed, similar performance with luminous power efficiency at maximum luminance

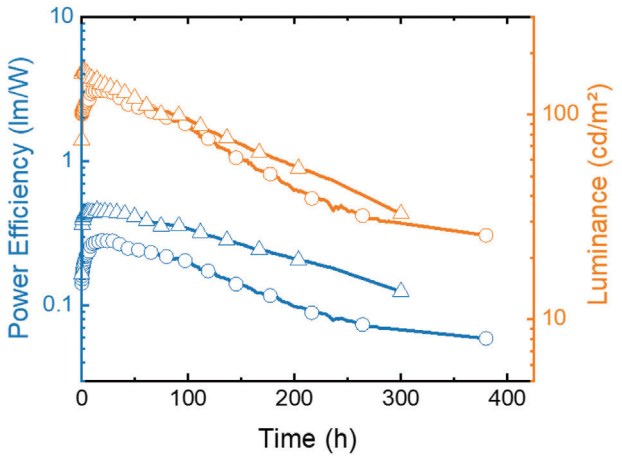

Figure 6. Luminance (orange) and luminous power efficiency (blue) for **MeOG2TAZ:CA-THA**-based LECs with glass/graphene (circles) or glass/ITO (triangles) anode measured using a pulsed current of 100 mA cm^{-2}.

of 0.3 lm W^{-1}@130 cd m^{-2} and 0.4 lm W^{-1}@165 cd m^{-2} stable for around 130 h are achieved for ITO-free and traditional LECs, respectively. All-in-all, the aforementioned on par performance in Dendri-LECs with biogenic electrolytes represents a promising step-forward to meet sustainable goals.

3. Conclusion

This work sets in the Dendri-LECs family with the first rationalization for implementing and optimizing TADF dendrimer emitters in combination with traditional and biogenic electrolytes as well as ITO and graphene electrodes. At first, the impact of the peripheral groups attached to two novel dendrimers on their spectroscopical, electrochemical, morphological, and ion conductivity features of thin-films has been thoughtfully rationalized using steady-state and temperature dependent time-resolved emission spectroscopy, cyclic voltammetry, AFM, and EIS, respectively. In short, the use of more electron donating hydrophilic pending groups , i.e., reference tert -butyl for methoxy, leads to i) a shift of the emission band from the green to the yellow region,ii) a TADF emission mechanism with a reduced PLQY (from 60% to ≈30%), iii) a more stable electrochemical behavior, and *iv)* a higher compatibility with biogenic electrolytes, showing enhanced dielectric and ion conductivities. This resulted in devices with a slightly reduced luminous power efficiency and brightness (3.2 lm W^{-1}@55 cd m^{-2}), but a strong enhanced stability of 98.3 J and 428 h@100 cd m^{-2} compared to reference Dendri-LECs, i.e., 4.0 lm W^{-1}@110 cd m^{-2} with stabilities of 5.7 J and 103 h@100 cd m^{-2}. What is more, the calculated device stability at 100 cd m^{-2} is among the best reported for archetypal yellow emitters, such as unsustainable Ir(III) complexes[36–38,63] and very expensive CPs,[34,35] Figure 1. In stark contrast, dendrimers provide benefits of a controllable synthesis, high solubility, easy upscaling, and low-cost, while device efficiency could be further maximized by i) stabilizing the position of the emitting neutral zone, ii) reducing microcavity effects, and iii) increasing light-outcoupling with microstructured electrodes and substrates, among others.[14] Finally, the Dendri-LEC performance hold using ITO-free LECs with graphene-based electrodes and novel biogenic cellulose-based electrolytes[13] highlighting their potential to realize truly sustainable and highly stable lighting devices in the near future. Overall, this work shows a fresh rationale that strongly reinforces the relevance of dendrimer-based materials for lighting purposes.

4. Experimental Section

Synthesis of 2,4,6-tris(4-(3,3"",6,6""-tetramethoxy-9"H-[9,3":6",9""-tercarbazol]-9"-yl)phenyl)-1,3,5-triazine (MeOG2TAZ): All chemicals were purchased from Kanto Kagaku Co., Ltd., TCI chemicals, Aldrich, or FUJIFILM Wako Chemicals without further purification. Dehydrated 1,4-dioxane was purchased from FUJIFILM Wako Chemicals and used without further purification. MeOG2on (second generation carbazole dendron with MeO terminal group) was synthesized according to the literature.[42] 2,4,6-tris(4-iodophenyl)-1,3,5-triazine (I3TAZ) was prepared according to the literature from 4-Iodobenzonitrile and trifluoromethanesulfonic acid.[2]

The ^{1}H and ^{13}C NMR spectra were obtained using a JEOL JNM-ECA 600 with TMS as the internal standard. The mass spectra were acquired by using JMS-700 (JMS-700, JEOL) with 3-NBA as the matrix in the positive ion mode. The Microwave reactions were performed using a Biotage Initiator^{+}. A preparative scale gel permeation chromatograph, LC-5060 (Japan Analytical Industry Co., Ltd.), was used to isolate each compound with chloroform as eluent.

MeOG2on (495 mg, 0.80 mmol), 2,4,6-tris(4-iodophenyl)-1,3,5-triazine (158 mg, 0.23 mmol), CuI (6.80 mg, 0.03 mmol), K_3PO_4 (454 mg, 2.14 mmol), (±)-*trans*-1,2-cyclohexanediamine (10.0 µL, 0.09 mmol), and dioxane (5.0 mL) were heated with microwave at 160 °C for 2 h under nitrogen atmosphere. The reaction mixture was diluted with toluene, and filtered through silica gel. The product was isolated by preparative GPC (eluent: chloroform). Yield: 66% (327 mg, 0.15 mmol).

^{1}H-NMR (600 MHz, $CDCl_3$) δ 9.21 (d, J = 8.2 Hz, 6H), 8.31 (d, J = 2.1 Hz, 6H), 8.03 (d, J = 8.2 Hz, 6H), 7.81 (d, J = 8.9 Hz, 6H), 7.65 (dd, J = 8.6, 1.7 Hz, 6H), 7.59 (d, J = 2.7 Hz, 12H), 7.34 (d, J = 8.9 Hz, 12H), 7.05 (dd, J = 8.9, 2.1 Hz, 12H), 3.96 (s, 36H)

^{13}C-NMR (600 MHz, $CDCl_3$): δ 171.2, 153.9, 141.4, 139.8, 137.2, 135.2, 131.4, 131.0, 126.9, 126.2, 124.4, 123.4, 119.5, 115.2, 111.3, 110.5, 102.9, 56.1

FAB-MS Calcd: $C_{141}H_{102}N_{12}O_{12}$ [M^{+}] 2154.7740, Found: 2154.7745.

Spectroscopic, Electrochemical, and Microscopy Characterization: All the solvents were obtained from a solvent purification system (M-BRAUN MB SPS-800). Cyclic voltammetry measurements were carried out in a cylindrical one-compartment cell with a three-electrode set-up. A Pt disk working electrode with a diameter of 3.0 mm, a Pt wire as counter and Ag wire as quasireference electrodes were used. Prior to every measurement, the working electrode was polished with Alumina slurry 0.04 mm from Schmitz Metallographie GmbH. The potential was controlled by a Metrohm µAutolabIII potentiostat. All measurements were conducted at 100 mV s^{-1} under inert nitrogen atmosphere with dry and degassed dimethylformamide (DMF) containing 0.1 M tetrabutylammonium hexafluorophosphate as supporting electrolyte. Ferrocene was added as internal standard to reference the acquired data to $Cp_2Fc^{+/0}$.

UV–Vis spectra in solution were recorded on a Shimadzu UV–Vis/2600spectrophotometer. The PL spectra and PLQY values at 300 K were measured with an FS5 Spectrofluorometer with an integrating sphere for absolute photoluminescence quantum yield valuation (Edinburgh Instruments). The integrating sphere was flushed with nitrogen before acquiring the measurements. Photoluminescence measurements at temperatures ranging from 77 to 300 K were performed upon enclosing the thin films in an Optistat-DN (Oxford Instruments) equipped with a temperature controller. Excited state decay lifetimes (τ) were obtained either with a microsecond flashlamp (λ_{exc} 305 nm, 100 Hz) or with picosecond laser (λ_{exc} 372 nm). The photoluminescence spectra

were acquired 10 min after the sample reached the desired temperature in order to ensure complete sample thermalization. The average lifetime can be obtained with the following formula

$$\langle \tau \rangle = \frac{A_1\tau_1^2 + A_2\tau_2^2}{A_1\tau_1 + A_2\tau_2} \quad (1)$$

Thin films were prepared from a filtered master solution of the desired compound (15 mg mL^{-1} in tetrahydrofuran or cyclohexanone) using a spin-coated technique at 1500 rpm for 30 s on quartz slides.

Topography images were acquired with MFP-3D Origin+ AFM (Asylum Research) and they were elaborated with Gwyddion evaluation software.

Graphene Growth and Transfer: To fabricate the multilayer graphene electrode, three sheets of wafer scale CVD graphene are synthesized and then stacked on top of each other using a semidry transfer method with polymethyl methacrylate (PMMA) as a support layer. The Raman spectra where obtained on a home built confocal Raman system with a 532 nm excitation laser and a grating width 1200 lines mm^{-1} installed in a spectrometer (Andor Shamrock) with a focal length of 500 mm and a deeply cooled CCD detector (iDUS). A laser power of 50 mW was used with and acquisition time of 3 s.

Device Fabrication and Measurement: ITO substrates were purchased from Naranjo Substrates with an ITO thickness of 130 nm. They were extensively cleaned using detergent, water, ethanol, and propan-2-ol as solvents in an ultrasonic bath (frequency 37–70 Hz) for 15 min each. Afterward, the slides were dried, and they were positioned in UV–ozone cleaner for 8 min. The clean plates were coated with 50 nm PEDOT:PSS layers via spin-coating. To this end, an aqueous solution of PEDOT:PSS was filtered and mixed with propan-2-ol in a ratio of 3:1. From this solution, 50 µL was dropped onto the substrate at a rotation speed of 2000 rpm and spun for 60 s. With regard of glass/graphene substrates, 150 nm thick layer was obtained via spray coating of PEDOT:PSS solution with a commercial airbrush: N_2 flow at 1 atm, 15 cm distance, and 30 s spraying time. In both cases, the resulting layers were dried on a hotplate at 120 °C. Stock solutions of dendrimers, $THABF_4$, PS (M_w ≈400 000), CA (M_w ≈30 000) were prepared in tetrahydrofuran or cyclohexanone at a concentration of 15 mg mL^{-1} for the emitters, 20 mg mL^{-1} for the salt, and 10 mg mL^{-1} for the polymers. Active layers (70–80 nm) were deposited from a sample solution, achieved by combining the corresponding stock solutions in the desired ratio (i.e., emitter:polymer:salt 1:0.1:0.2 and 1:0.2:0.2 in mass ratio for PS-THA and CA-THA, respectively), spin-coated at 1500 rpm for 30 s. In all cases, after the deposition of the active layer, the devices were dried under vacuum for 2 h and transferred to an inert atmosphere glovebox (<0.1 ppm O_2 and H_2O, Angstrom Engineering). Finally, aluminum cathodes (90 nm) were thermally evaporated onto the active layer using a shadow mask under high vacuum ($<1 \times 10^{-6}$ mbar) in an Angstrom Covap evaporator integrated into the inert atmosphere glovebox. Time dependence of luminance, voltage, and current was measured by applying pulsed voltage and monitoring the desired parameters simultaneously using an Avantes spectrophotometer (Avaspec- ULS2048L-USB2) in conjunction with a calibrated integrated sphere Avasphere 30-Irrad and Botest OLT OLED Lifetime-Test System. EIS assays were carried out with a potentiostat/galvanostat (Metrohm µAutolabIII) equipped with a frequency response analyzer module (FRA2). Measurements were performed at the applied voltage range from 0 to 4 V and fitted with the Nova software using the circuit model shown in Figure S11, Supporting Information. The AC signal amplitude was set to 10 mV and modulated in a frequency range from 10^0 to 10^6 Hz. The CPE element was typically used to consider i) the surface roughness of the electrodes and active layers, *ii)* inhomogeneous growing of the doped fronts using different active layer compositions and driving conditions, and *iii)* nonuniform electric field and/or current distribution across the active layer due to the morphology and thickness of the active layers. Ionic conductivity and dielectric constant were extrapolated from the fitted data following the procedure reported elsewhere.[27]

Statistical Analysis: Thin films statistic involve three replicates for each composition, while the device statistics involve up to five different devices, i.e., a total number of 20 pixels. The absence of outliers had been confirmed via *t*-test. The software OriginPro 2020b has been used for data analysis and evaluation.

Supporting Information

Supporting Information is available from the Wiley Online Library or from the author.

Acknowledgements

L.M.C., R.D.C., V.C., and R.R. acknowledged the European Union's innovation FET-OPEN under grant agreement MSCA-ITN STiBNite No. 956923. R.R. and D.W. acknowledged funding from the European Union's Horizon 2020 research and innovation programme under Grant Agreement SPRING No. 881273. K.Y. and K. A. acknowledged the support from JSPS KAKENHI Grant Nos. JP21H05399, JP20KK0316, and JP20H02801. K.A. also acknowledged the support from Grant-in-Aid for "'2019 Initiative for Realizing Diversity in the Research Environment"' through the "'Diversity and Super Global Training Program for Female and Young Faculty (SENTAN-Q),"' Kyushu University from MEXT, and Transdisciplinary Energy Research (Q-PIT) through its "'ModuleResearch Program."'

Open access funding enabled and organized by Projekt DEAL.

Conflict of Interest

The authors declare no conflict of interest.

Data Availability Statement

The data that support the findings of this study are available from the corresponding author upon reasonable request.

Keywords

dendrimers, electroluminescence, graphene electrodes, light-emitting electrochemical cells, thermally activated delayed fluorescence

Received: March 3, 2023
Revised: April 9, 2023
Published online: May 16, 2023

[1] B. Helms, E. W. Meijer, *Science* **2006**, *313*, 929.
[2] K. Albrecht, K. Matsuoka, K. Fujita, K. Yamamoto, *Angew. Chem., Int Ed.* **2015**, *54*, 5677.
[3] K. Albrecht, Y. Kasai, A. Kimoto, K. Yamamoto, *Macromolecules* **2008**, *41*, 3793.
[4] S. Gambino, S. G. Stevenson, K. A. Knights, P. L. Burn, I. D. W. Samuel, *Adv. Funct. Mater.* **2009**, *19*, 317.
[5] K. Albrecht, K. Yamamoto, *J. Am. Chem. Soc.* **2009**, *131*, 2244.
[6] Y. Li, G. Xie, S. Gong, K. Wu, C. Yang, *Chem. Sci.* **2016**, *7*, 5441.
[7] X. Wang, J. Hu, J. Lv, Q. Yang, H. Tian, S. Shao, L. Wang, X. Jing, F. Wang, *Angew. Chem., Int. Ed.* **2021**, *60*, 16585.
[8] H. Uoyama, K. Goushi, K. Shizu, H. Nomura, C. Adachi, *Nature* **2012**, *492*, 234.
[9] D. Sun, E. Duda, X. Fan, R. Saxena, M. Zhang, S. Bagnich, X. Zhang, A. Köhler, E. Zysman-Colman, *Adv. Mater.* **2022**, *34*, 2110344.
[10] C. Li, A. K. Harrison, Y. Liu, Z. Zhao, C. Zeng, F. B. Dias, Z. Ren, S. Yan, M. R. Bryce, *Angew. Chem., Int. Ed.* **2022**, *61*, e202115140.

[11] T. Sakanoue, F. Yonekawa, K. Albrecht, K. Yamamoto, T. Takenobu, *Chem. Mater.* **2017**, *29*, 6122.
[12] E. Fresta, R. D. Costa, *J. Mater. Chem. C* **2017**, *5*, 5643.
[13] L. M. Cavinato, G. Millán, J. Fernández-Cestau, E. Fresta, E. Lalinde, J. R. Berenguer, R. D. Costa, *Adv. Funct. Mater.* **2022**, *32*, 2201975.
[14] J. Ràfols-Ribé, X. Zhang, C. Larsen, P. Lundberg, E. M. Lindh, C. T. Mai, J. Mindemark, E. Gracia-Espino, L. Edman, *Adv. Mater.* **2022**, *34*, 2107849.
[15] Z. Zhang, K. Guo, Y. Li, X. Li, G. Guan, H. Li, Y. Luo, F. Zhao, Q. Zhang, B. Wei, Q. Pei, H. Peng, *Nat. Photonics* **2015**, *9*, 233.
[16] K. Hong, Y. K. Kwon, J. Ryu, J. Y. Lee, S. H. Kim, K. H. Lee, *Sci. Rep.* **2016**, *6*, 29805.
[17] K. G. Cho, J. I. Lee, S. Lee, K. Hong, M. S. Kang, K. H. Lee, *Adv. Funct. Mater.* **2020**, *30*, 1907936.
[18] K. Schlingman, Y. Chen, R. S. Carmichael, T. B. Carmichael, *Adv. Mater.* **2021**, *33*, 2006863.
[19] E. Fresta, A. Charisiadis, L. M. Cavinato, N. Palandjian, K. Karikis, V. Nikolaou, G. Charalambidis, A. G. Coutsolelos, R. D. Costa, *Adv. Photonics Res.* **2021**, *2*, 2000188.
[20] K. Youssef, Y. Li, S. O'Keeffe, L. Li, Q. Pei, *Adv. Funct. Mater.* **2020**, *30*, 1909102.
[21] L. M. Cavinato, S. Wölfl, A. Pöthig, E. Fresta, C. Garino, J. Fernandez-Cestau, C. Barolo, R. D. Costa, *Adv. Mater.* **2022**, *34*, 2109228.
[22] S. Keller, A. Prescimone, H. Bolink, M. Sessolo, G. Longo, L. Martínez-Sarti, J. M. Junquera-Hernández, E. C. Constable, E. Ortí, C. E. Housecroft, *Dalt. Trans.* **2018**, *47*, 14263.
[23] E. Fresta, M. D. Weber, J. Fernandez-Cestau, R. D. Costa, *Adv. Opt. Mater.* **2019**, *7*, 1900830.
[24] R. Bai, X. Meng, X. Wang, L. He, *Adv. Funct. Mater.* **2020**, *30*, 1907169.
[25] S. Tang, W.-Y. Tan, X.-H. Zhu, L. Edman, *Chem. Commun.* **2013**, *49*, 4926.
[26] Z. B. Hill, D. B. Rodovsky, J. M. Leger, G. P. Bartholomew, *Chem. Commun.* **2008**, *48*, 6594.
[27] E. Fresta, J. Dosso, J. Cabanillas-González, D. Bonifazi, R. D. Costa, *Adv. Funct. Mater.* **2020**, *30*, 1906830.
[28] E. Fresta, K. Baumgärtner, J. Cabanillas-Gonzalez, M. Mastalerz, R. D. Costa, *Nanoscale Horiz.* **2020**, *5*, 473.
[29] M. D. Weber, M. Adam, R. R. Tykwinski, R. D. Costa, *Adv. Funct. Mater.* **2015**, *25*, 5066.
[30] M. D. Weber, J. E. Wittmann, A. Burger, O. B. Malcıoğlu, J. Segarra-Martí, A. Hirsch, P. B. Coto, M. Bockstedte, R. D. Costa, *Adv. Funct. Mater.* **2016**, *26*, 6737.
[31] S. Tang, P. Lundberg, Y. Tsuchiya, J. Ràfols-Ribé, Y. Liu, J. Wang, C. Adachi, L. Edman, *Adv. Funct. Mater.* **2022**, *32*, 2205967.
[32] P. Lundberg, Y. Tsuchiya, E. M. Lindh, S. Tang, C. Adachi, L. Edman, *Nat. Commun.* **2019**, *10*, 5307.
[33] K. Albrecht, K. Matsuoka, D. Yokoyama, Y. Sakai, A. Nakayama, K. Fujita, K. Yamamoto, *Chem. Commun.* **2017**, *53*, 2439.
[34] S. Tang, J. Pan, H. Buchholz, L. Edman, *ACS Appl. Mater. Interfaces* **2011**, *3*, 3384.
[35] A. Asadpoordarvish, A. Sandström, S. Tang, J. Granström, L. Edman, *Appl. Phys. Lett.* **2012**, *100*, 193508.
[36] L. He, L. Duan, J. Qiao, D. Zhang, L. Wang, Y. Qiu, *Chem. Commun.* **2011**, *47*, 6467.
[37] J. E. Namanga, H. Pei, G. Bousrez, B. Mallick, V. Smetana, N. Gerlitzki, A. Mudring, *Adv. Funct. Mater.* **2020**, *30*, 1909809.
[38] C. D. Ertl, C. Momblona, A. Pertegás, J. M. Junquera-Hernández, M.-G. La-Placa, A. Prescimone, E. Ortí, C. E. Housecroft, E. C. Constable, H. J. Bolink, *J. Am. Chem. Soc.* **2017**, *139*, 3237.
[39] D. Tordera, S. Meier, M. Lenes, R. D. Costa, E. Ortí, W. Sarfert, H. J. Bolink, *Adv. Mater.* **2012**, *24*, 897.
[40] C. Li, C. F. R. Mackenzie, S. A. Said, A. K. Pal, M. A. Haghighatbin, A. Babaei, M. Sessolo, D. B. Cordes, A. M. Z. Z. Slawin, P. C. J. J. Kamer, H. J. Bolink, C. F. Hogan, E. Zysman-Colman, *Inorg. Chem.* **2021**, *60*, 10323.
[41] A. Mishra, M. Alahbakhshi, R. Haroldson, L. D. Bastatas, Q. Gu, A. A. Zakhidov, J. D. Slinker, *Adv. Opt. Mater.* **2020**, *8*, 2000226.
[42] K. Matsuoka, K. Albrecht, A. Nakayama, K. Yamamoto, K. Fujita, *ACS Appl. Mater. Interfaces* **2018**, *10*, 33343.
[43] L. Micaroni, F. C. Nart, I. A. Hümmelgen, *J. Solid State Electrochem.* **2002**, *7*, 55.
[44] K. Goushi, K. Yoshida, K. Sato, C. Adachi, *Nat. Photonics* **2012**, *6*, 253.
[45] D. Levy, D. Avnir, *J. Photochem. Photobiol. A: Chem.* **1991**, *57*, 41.
[46] T.-S. Fang, R. E. Brown, C. L. Kwan, L. A. Singer, *J. Phys. Chem.* **1978**, *82*, 2489.
[47] M. W. Wolf, K. D. Legg, R. E. Brown, L. A. Singer, J. H. Parks, *J. Am. Chem. Soc.* **1975**, *97*, 4490.
[48] E. Fresta, G. U. Mahoro, L. M. Cavinato, J. Lohier, J. Renaud, S. Gaillard, R. D. Costa, *Adv. Opt. Mater.* **2022**, *10*, 2101999.
[49] R. Czerwieniec, K. Kowalski, H. Yersin, *Dalt. Trans.* **2013**, *42*, 9826.
[50] C. E. Housecroft, E. C. Constable, *J. Mater. Chem. C* **2022**, *10*, 4456.
[51] H. Kaji, H. Suzuki, T. Fukushima, K. Shizu, K. Suzuki, S. Kubo, T. Komino, H. Oiwa, F. Suzuki, A. Wakamiya, Y. Murata, C. Adachi, *Nat. Commun.* **2015**, *6*, 8476.
[52] K. Masui, H. Nakanotani, C. Adachi, *Org. Electron.* **2013**, *14*, 2721.
[53] N. Haase, A. Danos, C. Pflumm, A. Morherr, P. Stachelek, A. Mekic, W. Brütting, A. P. Monkman, *J. Phys. Chem. C* **2018**, *122*, 29173.
[54] F. B. Dias, T. J. Penfold, A. P. Monkman, *Methods Appl. Fluoresc.* **2017**, *5*, 012001.
[55] M. N. Berberan-Santos, J. M. M. Garcia, *J. Am. Chem. Soc.* **1996**, *118*, 9391.
[56] D. Kelly, L. G. Franca, K. Stavrou, A. Danos, A. P. Monkman, *J. Phys. Chem. Lett.* **2022**, *13*, 6981.
[57] M. Karaman, A. Kumar Gupta, S. Madayanad Suresh, T. Matulaitis, L. Mardegan, D. Tordera, H. J. Bolink, S. Wu, S. Warriner, I. D. Samuel, E. Zysman-Colman, *Beilstein J. Org. Chem.* **2022**, *18*, 1311.
[58] Z. Yang, H. Su, *Adv. Funct. Mater.* **2020**, *30*, 1906788.
[59] S. B. Anantharaman, S. Yakunin, C. Peng, M. V. G. Vismara, C. F. O. Graeff, F. A. Nüesch, S. Jenatsch, R. Hany, M. V. Kovalenko, J. Heier, *J. Phys. Chem. C* **2017**, *121*, 9587.
[60] S. T. Parker, J. D. Slinker, M. S. Lowry, M. P. Cox, S. Bernhard, G. G. Malliaras, *Chem. Mater.* **2005**, *17*, 3187.
[61] M. Diethelm, A. Schiller, M. Kawecki, A. Devižis, B. Blülle, S. Jenatsch, E. Knapp, Q. Grossmann, B. Ruhstaller, F. Nüesch, R. Hany, *Adv. Funct. Mater.* **2020**, *30*, 1906803.
[62] P. Sharif, E. Alemdar, S. Ozturk, O. Caylan, T. Haciefendioglu, G. Buke, M. Aydemir, A. Danos, A. P. Monkman, E. Yildirim, G. Gunbas, A. Cirpan, A. Oral, *Adv. Funct. Mater.* **2022**, *32*, 2207324.
[63] Y. Shen, D. D. Kuddes, C. A. Naquin, T. W. Hesterberg, C. Kusmierz, B. J. Holliday, J. D. Slinker, *Appl. Phys. Lett.* **2013**, *102*, 203305.